

# Extending the Electrochemical Window of Na<sup>+</sup> Halide Nanocomposite Solid Electrolytes for 5 V-Class All-Solid-State Na-Ion Batteries

Juhyoun Park,<sup>1</sup> Daseul Han,<sup>1</sup> Jun Pyo Son, Hiram Kwak, Wonseok Ko, Changhyun Park, Chanhee Lee, Hyun-Wook Lee, Jongsoon Kim, Kyung-Wan Nam,\* and Yoon Seok Jung\*



Cite This: *ACS Energy Lett.* 2024, 9, 2222–2230



Read Online

ACCESS |



Metrics & More

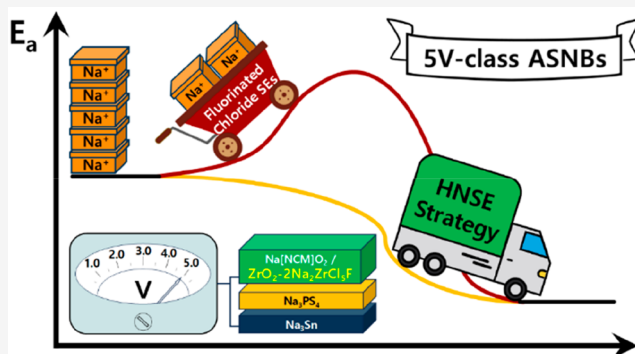


Article Recommendations



Supporting Information

**ABSTRACT:** This study introduces a Na<sup>+</sup> fluorinated halide nanocomposite solid electrolyte (HNSE), ZrO<sub>2</sub>-2Na<sub>2</sub>ZrCl<sub>5</sub>F, synthesized through a mechanochemical reaction using Na<sub>2</sub>O. This HNSE exhibits a substantial improvement in Na<sup>+</sup> conductivity ( $2.1 \times 10^{-5}$  S cm<sup>-1</sup> at 30 °C) compared to Na<sub>2</sub>ZrCl<sub>5</sub>F ( $2.0 \times 10^{-7}$  S cm<sup>-1</sup>). The significant reduction in ionic conductivity of Na<sub>2</sub>ZrCl<sub>5</sub>F relative to Na<sub>2</sub>ZrCl<sub>6</sub> ( $2.0 \times 10^{-5}$  S cm<sup>-1</sup>) is elucidated through synchrotron pair distribution function (PDF) analysis. Structural insights, including the fine structure of the ZrO<sub>2</sub> nanograins embedded in an amorphous Na<sub>2</sub>ZrCl<sub>5</sub>F matrix and the potential O-substituted interphase, are revealed through X-ray absorption spectroscopy, PDF, and cryogenic transmission electron microscopy. Fluorinated HNSEs offer exceptional electrochemical oxidative stability up to 5 V (vs Na/Na<sup>+</sup>), enabling high-voltage cathode applications. Na<sub>0.66</sub>Ni<sub>0.1</sub>Co<sub>0.1</sub>Mn<sub>0.8</sub>O<sub>2</sub>||Na<sub>3</sub>Sn all-solid-state cells using ZrO<sub>2</sub>-2Na<sub>2</sub>ZrCl<sub>5</sub>F as the catholyte demonstrate enhanced performance at 30 °C compared to cells using Na<sub>2</sub>ZrCl<sub>6</sub> (47.4% capacity retention after 100 cycles vs 35.3% using Na<sub>2</sub>ZrCl<sub>6</sub>).



The expansion of lithium-ion batteries (LIBs) into large-scale applications, such as electric vehicles (kWh) and energy storage systems (>MWh),<sup>1–3</sup> is challenged by the unstable global supply chain of Li, which is exacerbated by environmental and political issues.<sup>4–6</sup> Safety concerns owing to flammable organic liquid electrolytes in LIBs further complicate their use.<sup>7–10</sup> All-solid-state Na-ion or Na batteries (ASNBS) with inorganic solid electrolytes (SEs) offer a promising alternative solution to these problems.<sup>11–16</sup>

Several types of inorganic Na<sup>+</sup> conducting SEs have been explored for ASNBS, including oxides (e.g., Na<sub>3</sub>Zr<sub>2</sub>Si<sub>2</sub>PO<sub>12</sub>,  $\sim 10^{-3}$  S cm<sup>-1</sup>),<sup>17</sup> sulfides (e.g., Na<sub>3</sub>PnS<sub>4</sub>, Pn = P, Sb, max.  $\sim 10^{-2}$  S cm<sup>-1</sup>),<sup>11,18–23</sup> halides (e.g., Na<sub>2</sub>ZrCl<sub>6</sub>,  $\sim 10^{-5}$  S cm<sup>-1</sup>),<sup>24,25</sup> and closo-borates (e.g., Na<sub>2</sub>(B<sub>10</sub>H<sub>10</sub>)<sub>0.5</sub>(B<sub>12</sub>H<sub>12</sub>)<sub>0.5</sub>,  $\sim 10^{-3}$  S cm<sup>-1</sup>).<sup>26</sup> Among these, halide SEs are notable candidates owing to the electrochemical oxidative stability of oxides and the mechanical deformability of sulfides.<sup>24,25,27–35</sup> Since the seminal report of trigonal Li<sub>3</sub>YCl<sub>6</sub> and monoclinic Li<sub>3</sub>YBr<sub>6</sub>, which exhibited impressive Li<sup>+</sup> conductivities of 0.51 and 1.7 mS cm<sup>-1</sup>, respectively,<sup>27</sup> the reignited investigation of halide SEs has resulted in the identification of novel compounds,<sup>25,36</sup> including the Li<sub>x</sub>MCl<sub>6</sub> family ( $x = 2$  or 3),

such as Li<sub>3</sub>YCl<sub>6</sub> (0.51 mS cm<sup>-1</sup>),<sup>27</sup> Li<sub>2</sub>ZrCl<sub>6</sub> (0.40 mS cm<sup>-1</sup>),<sup>31</sup> Li<sub>3</sub>YbCl<sub>6</sub> (0.14 mS cm<sup>-1</sup>),<sup>32</sup> Li<sub>3</sub>InCl<sub>6</sub> (1.49 mS cm<sup>-1</sup>),<sup>37</sup> and Li<sub>3</sub>ScCl<sub>6</sub> (3 mS cm<sup>-1</sup>).<sup>38</sup>

In solid-state chemistry, elemental substitution is a common technique for controlling charge-carrier concentration or structural framework, which enhances the ionic conductivity of superionic conductors. This approach is effective for halide SEs, as demonstrated for various compounds, including Li<sub>3–x</sub>M<sub>1–x</sub>Zr<sub>x</sub>Cl<sub>6</sub> (M = Y, Er,<sup>39</sup> max. 1.4 mS cm<sup>-1</sup>; M = In, Sc,<sup>34</sup> max. 2.1 mS cm<sup>-1</sup>), Li<sub>2+x</sub>Zr<sub>1–x</sub>M<sub>x</sub>Cl<sub>6</sub> (M = Fe, Cr, V, max. 1.0 mS cm<sup>-1</sup>),<sup>31</sup> and Li<sub>3–x</sub>Yb<sub>1–x</sub>M<sub>x</sub>Cl<sub>6</sub> (M = Zr, Hf, max. 1.5 mS cm<sup>-1</sup>).<sup>32</sup> In addition, the choice of preparation methods, particularly mechanochemical preparation, significantly impacts the microstructures of halide SEs, particularly in terms of

Received: February 16, 2024

Revised: March 28, 2024

Accepted: April 8, 2024

Published: April 15, 2024



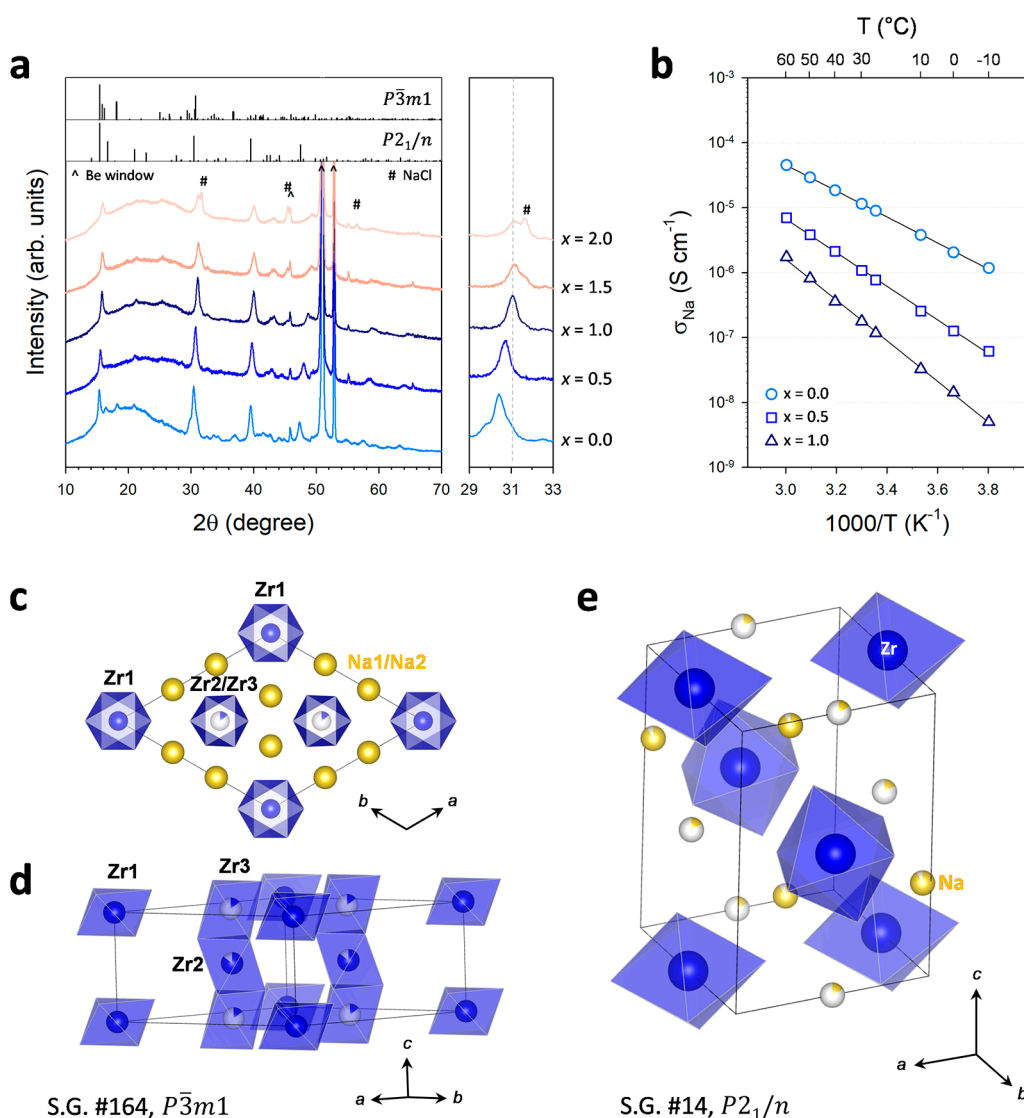


**Figure 1.** Characterization of fluorinated  $\text{Na}_2\text{ZrCl}_6$  ( $\text{Na}_2\text{ZrCl}_{6-x}\text{F}_x$ ). (a) XRD patterns and (b) Arrhenius plots of  $\text{Na}^+$  conductivities of  $\text{Na}_2\text{ZrCl}_{6-x}\text{F}_x$ . Crystal structures of (c and d)  $P\bar{3}m1$  and (e)  $P2_1/n$ .

structural disorder and metal distributions, which consequently affect their ionic conductivity.<sup>40,41</sup> While fewer  $\text{Na}^+$  halide SEs have been identified compared to their  $\text{Li}^+$  counterparts, their development has followed similar patterns.<sup>25</sup>

$\text{Na}^+$  halide SEs developed via composition tuning include  $\text{Na}_{3-x}\text{Er}_{1-x}\text{Zr}_x\text{Cl}_6$  ( $0.04 \text{ mS cm}^{-1}$ ),<sup>42</sup>  $\text{Na}_{3-x}\text{Y}_{1-x}\text{Zr}_x\text{Cl}_6$  ( $0.066 \text{ mS cm}^{-1}$ ),<sup>43</sup>  $\text{Na}_{3-x}\text{Yb}_{1-x}\text{Zr}_x\text{Cl}_6$  ( $0.066 \text{ mS cm}^{-1}$ ),<sup>44</sup>  $\text{Na}_{3-x}\text{Cr}_{1-x}\text{Zr}_x\text{Cl}_6$  ( $0.1 \text{ mS cm}^{-1}$ ),<sup>45</sup> and  $\text{Na}_{3-x}\text{In}_{1-x}\text{Zr}_x\text{Cl}_6$  ( $\sim 0.01 \text{ mS cm}^{-1}$ ).<sup>46</sup> A significant enhancement in ionic conductivity has been observed in several compounds prepared using the mechanochemical method, such as  $\text{Na}_2\text{ZrCl}_6$ ,  $\text{NaAlCl}_4$ , and  $\text{Na}_3\text{InCl}_6$ .<sup>16,24,29,46,47</sup> Specifically, ball-milled trigonal  $\text{Na}_2\text{ZrCl}_6$  with a  $P\bar{3}m1$  space group demonstrated a significant increase in ionic conductivity ( $1.8 \times 10^{-5} \text{ S cm}^{-1}$ ) compared to its annealed counterpart ( $6.9 \times 10^{-8} \text{ S cm}^{-1}$ ).<sup>24</sup> This difference in conductivity was presumed to stem from the occupation of an interstitial  $\text{Na}^+$  site in the (002) plane, regulating  $\text{Na}^+$  connectivity and thus the  $\text{Na}^+$  migration energy landscape in the lattice. In a separate observation, the ball-milled sample exhibited both  $P\bar{3}m1$  and  $P2_1/n$  structures,

unlike its annealed version, which exhibited only the  $P\bar{3}m1$  structure.<sup>47</sup> The inclusion of the  $P2_1/n$  structure in  $\text{Na}_2\text{ZrCl}_6$  facilitates isotropic  $\text{Na}^+$  migration pathways and intrinsic vacancies, leading to higher ionic conductivity.<sup>47</sup> For  $\text{NaAlCl}_4$ , a new Na site was identified in the mechanochemically prepared sample ( $3.9 \times 10^{-6} \text{ S cm}^{-1}$ ), a feature absent in the annealed sample ( $3.3 \times 10^{-7} \text{ S cm}^{-1}$ ).<sup>16</sup> This new site facilitates the formation of a net-like 2D ionic conduction pathway within the  $ac$ -plane. However, the advancement of halide-based ASNBs is often hindered by the limited ionic conductivities of several halide SEs, typically at approximately  $10^{-5} \text{ S cm}^{-1}$ ,<sup>24,25,42,43,48</sup> except for  $\text{NaAlCl}_{4-2x}\text{O}_x$  ( $1.3 \text{ mS cm}^{-1}$ )<sup>49</sup> and Ta-based materials ( $2.7$  and  $4.6 \text{ mS cm}^{-1}$  for  $0.5\text{Na}_2\text{O}_2\text{-TaCl}_5$  and  $x[\text{Na}_{0.75}(\text{La}/\text{Sm})_{1.75}\text{Cl}_6] \cdot (1-x)\text{-}[\text{NaTaCl}_6]$ , respectively).<sup>50,51</sup>

Our group recently demonstrated a novel method for ameliorating the ionic conductivity of halide SEs through interfacial conduction by using a nanocomposite strategy. Mechanochemical synthesis involving  $\text{Li}_2\text{O}$  or  $\text{Na}_2\text{O}$  has enabled the formation of partially O-substituted interphases

in halide nanocomposite SEs (HNSEs), significantly enhancing ionic conductivity from 0.40 to 1.3 mS cm<sup>-1</sup> for Li HNSEs (ZrO<sub>2</sub>-2LiCl-Li<sub>2</sub>ZrCl<sub>6</sub>) and from 0.011 to 0.11 mS cm<sup>-1</sup> for Na HNSEs (0.13ZrO<sub>2</sub>-0.61NaCl-0.26Na<sub>2</sub>ZrCl<sub>6</sub>).<sup>29</sup> However, the effectiveness of this strategy has yet to be investigated for fluorinated Na<sup>+</sup> halide SEs.

For practical applications, the prevalent use of rare and expensive central metals in halide SEs, such as Y, Sc, and In, poses a considerable challenge, with Al or Zr being the exceptions.<sup>16,24,25,31</sup> Recent theoretical and experimental investigations have emphasized the pivotal role of ternary (or quaternary) cations and halogen anions in determining the electrochemical stability of these SEs.<sup>28</sup> In particular, substituting Cl<sup>-</sup> with F<sup>-</sup> can extend the electrochemical oxidative limit. However, this advantage is offset by a decrease in the ionic conductivities. Moreover, the origins behind the decrease have not been clearly elucidated in relation to the crystal structure.<sup>52</sup> In the realm of Na<sup>+</sup> halide SEs, studies on enhancing the electrochemical stability of Na<sup>+</sup> chloride SEs are still lacking, specifically with the absence of cases for fluorinated Na<sup>+</sup> chloride SEs. Furthermore, while most previous studies on Na<sup>+</sup> halide SEs have focused on the 3 V-class NaCrO<sub>2</sub> cathode,<sup>16,24,43</sup> significant developments in various high-voltage Na<sup>+</sup> cathodes, such as Na-Fe<sub>0.55</sub>Mn<sub>0.44</sub>Nb<sub>0.01</sub>O<sub>2</sub> (2.0–4.0 V) and Na<sub>0.67</sub>Mg<sub>0.22</sub>Mn<sub>0.55</sub>Fe<sub>0.23</sub>O<sub>2</sub> (2.0–4.5 V) also occurred.<sup>53,54</sup> Therefore, developing high-voltage halide Na<sup>+</sup> SEs to complement these cathode advancements is essential.

In this study, we present a new Na<sup>+</sup> halide SE comprising ZrO<sub>2</sub> and fluorinated Na<sub>2</sub>ZrCl<sub>5</sub>F nanograins, which significantly improved Na<sup>+</sup> conductivity (2.1 × 10<sup>-5</sup> S cm<sup>-1</sup> at 30 °C) compared to pure Na<sub>2</sub>ZrCl<sub>5</sub>F (2.0 × 10<sup>-7</sup> S cm<sup>-1</sup>). To the best of our knowledge, this is the first development of fluorinated Na<sup>+</sup> chloride SEs. The fluorinated HNSEs were synthesized via a mechanochemical reaction using Na<sub>2</sub>O. Cryogenic scanning transmission electron microscopy (cryo-STEM) revealed nanostructures featuring ZrO<sub>2</sub> nanoparticles embedded within an amorphous Na<sub>2</sub>ZrCl<sub>5</sub>F matrix. Combined synchrotron X-ray pair distribution function (PDF) and X-ray absorption spectroscopy (XAS) comprehensively elucidated the fine structures of Na<sub>2</sub>ZrCl<sub>6</sub> and Na<sub>2</sub>ZrCl<sub>5</sub>F, as well as the causes for the substantial decrease in Na<sup>+</sup> conductivity by fluorination, specifically from the perspective of the crystal structure. Furthermore, the ZrO<sub>2</sub>-Na<sub>2</sub>ZrCl<sub>5</sub>F HNSE exhibited excellent electrochemical oxidative stability, reaching ~5 V (vs Na/Na<sup>+</sup>), rendering it suitable for high-voltage cathode applications. Its compatibility with a P2-type Na<sub>0.66</sub>Ni<sub>0.1</sub>Co<sub>0.1</sub>Mn<sub>0.8</sub>O<sub>2</sub> (NaNCM) in NaNCM||Na<sub>3</sub>Sn ASNBs operating in 1.5–5.0 V at 30 °C was successfully demonstrated.

To explore the extent of fluorination in Na<sub>2</sub>ZrCl<sub>6</sub>, Na<sub>2</sub>ZrCl<sub>6-x</sub>F<sub>x</sub> samples with *x* = 0.0, 0.5, 1.0, 1.5, and 2.0 were prepared by using the mechanochemical method. The X-ray diffraction (XRD) patterns of these samples revealed that the original trigonal P3m1 structure of Na<sub>2</sub>ZrCl<sub>6</sub> is retained across all variants (Figure 1a).<sup>24,43</sup> Specifically, up to *x* = 1.0, a gradual positive shift in the (301) peak at ~30.5° with no emerging impurity phases suggests a lattice contraction in Na<sub>2</sub>ZrCl<sub>6</sub>, which is attributed to the smaller ionic radius of F<sup>-</sup> (133 pm) compared to that of Cl<sup>-</sup> (181 pm).<sup>55</sup> However, at *x* ≥ 1.5, the evolution of NaCl indicated a fluorination limit between *x* = 1.0 and 1.5.

The Na<sup>+</sup> conductivities of the cold-pressed pellets were measured by using the AC impedance method with Na<sup>+</sup>-blocking TiSE|Ti symmetric cells. The corresponding Arrhenius plots for Na<sub>2</sub>ZrCl<sub>6-x</sub>F<sub>x</sub> (*x* = 0, 0.5, and 1.0) shown in Figure 1b indicate that fluorination substantially reduces the ionic conductivity of Na<sub>2</sub>ZrCl<sub>6</sub>, which is consistent with other fluorinated chloride compounds.<sup>29,52</sup> The ionic conductivity of Na<sub>2</sub>ZrCl<sub>6</sub> at 30 °C was 1.1 × 10<sup>-5</sup> S cm<sup>-1</sup>,<sup>43</sup> which decreased by 2 orders of magnitude to 2.0 × 10<sup>-7</sup> S cm<sup>-1</sup> upon fluorination (Na<sub>2</sub>ZrCl<sub>5</sub>F). The activation energy increased significantly from 0.398 to 0.605 eV. This substantially impeded Na<sup>+</sup> migration in fluorinated Na<sub>2</sub>ZrCl<sub>6</sub> can be explained by a simple Coulombic force consideration (eq 1), which is a stronger Coulombic attraction between Na<sup>+</sup> and the anion framework.

$$|F| = k_e \frac{|q_1 q_2|}{r^2} \quad (1)$$

where *k<sub>e</sub>* is the Coulombic constant, *q<sub>1</sub>* and *q<sub>2</sub>* are the magnitudes of the charges, and *r* is the distance between the charges.

The reduced lattice spacing due to fluorination implies a shorter distance between Na<sup>+</sup> and counteranions, resulting in stronger attractive forces that impede Na<sup>+</sup> migration in the channels.

Further, to deepen our understanding of the structure–transport relationship in fluorinated Na<sub>2</sub>ZrCl<sub>6</sub>, PDF curve fitting was performed on Na<sub>2</sub>ZrCl<sub>6</sub> and Na<sub>2</sub>ZrCl<sub>5</sub>F in the range of 1.5–20 Å, as depicted in Figure S1. In addition, the structures calculated from the best-fit results are shown in Figure S2, and the corresponding structural information is tabulated in Table S1. Na<sub>2</sub>ZrCl<sub>6</sub> was refined and revealed a composite structure, including the phases of P3m1 and P2<sub>1</sub>/n structures (Figure 1c–e), which is consistent with a previous report.<sup>42</sup> Notably, the trigonal P3m1 phase of Na<sub>2</sub>ZrCl<sub>6</sub> exhibited higher site disorder in Zr<sup>4+</sup> and Na<sup>+</sup> sites compared to Na<sub>2</sub>ZrCl<sub>5</sub>F (Figure S2), reflecting a controlled energy landscape that promotes enhanced Na<sup>+</sup> migration.<sup>40</sup> In contrast, Na<sub>2</sub>ZrCl<sub>5</sub>F was solely in the P3m1 phase, without the inclusion of the P2<sub>1</sub>/n phase. Since the P2<sub>1</sub>/n phase has higher conductivity than P3m1 because of intrinsic vacancies and isotropic conduction pathways,<sup>47</sup> the absence of the P2<sub>1</sub>/n phase in Na<sub>2</sub>ZrCl<sub>5</sub>F essentially contributes to its lower Na<sup>+</sup> conductivity. To pinpoint the specific sites of F<sup>-</sup> and ascertain the occupation of Zr sites in Na<sub>2</sub>ZrCl<sub>5</sub>F, PDF fitting was conducted on symmetry-relaxed P3m1 structures, focusing on whether Zr occupied the Zr2 or Zr3 sites. The fitting results reveal that F<sup>-</sup> predominantly replaced the Cl sites in the ZrCl<sub>6</sub> polyhedra at the Zr2 and Zr3 sites, rather than those at the Zr1 site (Figure S2c,d). Notably, in Na<sub>2</sub>ZrCl<sub>5</sub>F, the Zr2 site occupancy is prevalent (72.9%) over the Zr3 site occupancy (24.9%). Additionally, the Na1 site (Wyckoff 6h) in the (002) plane exhibits a significantly high occupancy of 0.92 in the case of Zr2-occupied Na<sub>2</sub>ZrCl<sub>5</sub>F. These structural identifications explain the low ionic conductivity of Na<sub>2</sub>ZrCl<sub>5</sub>F, as the atomic arrangements with a lack of disorder in both metal and Na sites reflect inefficiency in Na<sup>+</sup> conduction within trigonal halide structure.<sup>40</sup> This is the first reported case demonstrating that metal site disorder influences the ionic conductivity in Na halide SEs. In summary, the 1/100 times decrease in Na<sup>+</sup> conductivity of Na<sub>2</sub>ZrCl<sub>5</sub>F compared to Na<sub>2</sub>ZrCl<sub>6</sub> is attributed to the preferential Zr2 site occupation and site-ordering in the

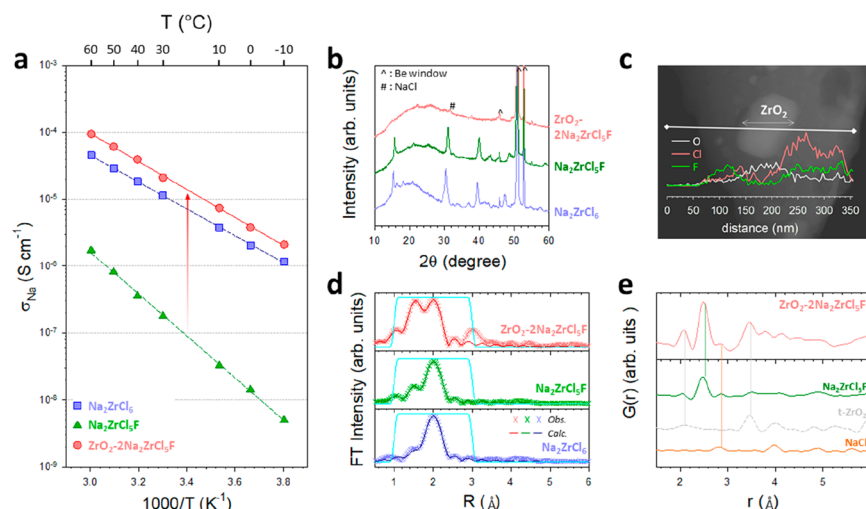
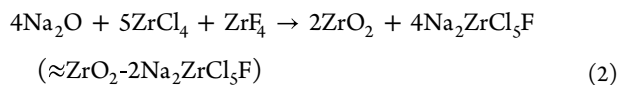


**Figure 2.** Characterization of  $\text{ZrO}_2\text{-}2\text{Na}_2\text{ZrCl}_5\text{F}$  HNSE. (a) Arrhenius plots of ionic conductivities and (b) XRD patterns of  $\text{ZrO}_2\text{-}2\text{Na}_2\text{ZrCl}_5\text{F}$  compared with conventional  $\text{Na}_2\text{ZrCl}_6$  and  $\text{Na}_2\text{ZrCl}_5\text{F}$ . (c) STEM EDXS line maps for  $\text{ZrO}_2\text{-}2\text{Na}_2\text{ZrCl}_5\text{F}$  HNSE. (d) EXAFS spectra of  $\text{ZrO}_2\text{-}2\text{Na}_2\text{ZrCl}_5\text{F}$ ,  $\text{Na}_2\text{ZrCl}_5\text{F}$ , and  $\text{Na}_2\text{ZrCl}_6$ . (e) PDF  $G(r)$  for  $\text{ZrO}_2\text{-}2\text{Na}_2\text{ZrCl}_5\text{F}$ , compared with references ( $\text{Na}_2\text{ZrCl}_5\text{F}$ , tetragonal  $\text{ZrO}_2$  (t- $\text{ZrO}_2$ ), and NaCl).

ordered  $P\bar{3}m1$  phase and the lack of a highly conductive  $P2_1/n$  phase.

To enhance the ionic conductivity of  $\text{Na}_2\text{ZrCl}_5\text{F}$ , the HNSE strategy was applied, which involved the mechanochemical reaction of  $\text{ZrCl}_4$  and  $\text{ZrF}_4$  with  $\text{Na}_2\text{O}$ , as shown in eq 2.



Specifically,  $\text{Na}_2\text{O}$  reacts with  $\text{ZrCl}_4$  (or  $\text{ZrF}_4$ ) to form  $\text{ZrO}_2$  nanoparticles alongside NaCl (or NaF). The remaining  $\text{ZrCl}_4$  and  $\text{ZrF}_4$  react with NaCl to yield  $\text{Na}_2\text{ZrCl}_5\text{F}$ . Figure 2a presents the Arrhenius plots, comparing the ionic conductivities of  $\text{Na}_2\text{ZrCl}_6$ ,  $\text{Na}_2\text{ZrCl}_5\text{F}$ , and  $\text{ZrO}_2\text{-}2\text{Na}_2\text{ZrCl}_5\text{F}$  HNSE. Nyquist plots of the  $\text{ZrO}_2\text{-}2\text{Na}_2\text{ZrCl}_5\text{F}$  HNSE at various temperatures are shown in Figure S3. Notably, compared to  $\text{Na}_2\text{ZrCl}_5\text{F}$ , the  $\text{Na}^+$  conductivity of the  $\text{ZrO}_2\text{-}2\text{Na}_2\text{ZrCl}_5\text{F}$  HNSE demonstrated a substantial increase of 2 orders of magnitude, from  $2.0 \times 10^{-7}$  to  $2.1 \times 10^{-5} \text{ S cm}^{-1}$ .

Furthermore,  $\text{ZrO}_2\text{-NaCl-Na}_2\text{ZrCl}_5\text{F}$  samples with varying  $\text{ZrO}_2$  volume fractions of 0 to 7 vol % were prepared. Table S2 lists the  $\text{Na}^+$  conductivities, recipes, and fractions of the samples. Fixed volume fractions of  $\text{Na}_2\text{ZrCl}_5\text{F}$  (93 vol %) were maintained, resulting in calculated  $\text{ZrO}_2$  volume fractions in  $\text{ZrO}_2\text{-}2\text{Na}_2\text{ZrCl}_5\text{F}$  and  $0.29\text{NaCl}\text{-}0.71\text{Na}_2\text{ZrCl}_5\text{F}$  of 7 vol % and 0 vol %, respectively. The  $0.29\text{NaCl}\text{-}0.71\text{Na}_2\text{ZrCl}_5\text{F}$  with the 7:93 (NaCl/ $\text{Na}_2\text{ZrCl}_5\text{F}$ ) vol. ratio exhibited the lowest ionic conductivity of  $9.5 \times 10^{-7} \text{ S cm}^{-1}$ . Although this value exceeded that of pure  $\text{Na}_2\text{ZrCl}_5\text{F}$ , the increase could be attributed to incomplete fluorination. Anion mixing between Cl in NaCl and F in  $\text{Na}_2\text{ZrCl}_5\text{F}$ , indicated by a shift in the XRD peak between  $\text{Na}_2\text{ZrCl}_6$  and  $\text{Na}_2\text{ZrCl}_5\text{F}$ , supports this interpretation, as shown in Figure S4. In contrast, all the samples containing  $\text{ZrO}_2$  (2.4, 4.9, and 7.0 vol %) exhibited high  $\text{Na}^+$  conductivities exceeding  $10^{-5} \text{ S cm}^{-1}$ , verifying the pivotal role of the interphase between  $\text{ZrO}_2$  and  $\text{Na}_2\text{ZrCl}_5\text{F}$ .

Figure 2b displays the XRD patterns of  $\text{Na}_2\text{ZrCl}_6$ ,  $\text{Na}_2\text{ZrCl}_5\text{F}$ , and  $\text{ZrO}_2\text{-}2\text{Na}_2\text{ZrCl}_5\text{F}$ . The  $\text{ZrO}_2\text{-}2\text{Na}_2\text{ZrCl}_5\text{F}$  HNSE exhibited no distinct peaks except for minor NaCl impurities, indicating poor crystallinity, nanograin formation,

or amorphization owing to partial O-substitution.<sup>29,49</sup> The presence of  $\text{ZrO}_2$  in the  $\text{ZrO}_2\text{-}2\text{Na}_2\text{ZrCl}_5\text{F}$  HNSE was further confirmed through cryo-STEM energy-dispersive X-ray spectroscopy (EDXS) mapping, as depicted in Figures 2c and S5. Specifically, the matrix exhibited high concentrations of F and Cl around the nanoparticles along with high-intensity Zr and O signals within the nanoparticles, confirming the embedding of  $\text{ZrO}_2$  nanoparticles in the  $\text{Na}_2\text{ZrCl}_5\text{F}$  matrix.

The local structure of the poorly crystalline  $\text{ZrO}_2\text{-}2\text{Na}_2\text{ZrCl}_5\text{F}$  HNSE was further probed by using synchrotron XAS and PDF analyses. The Zr K-edge X-ray absorption near-edge structure (XANES) and extended X-ray absorption fine structure (EXAFS) spectra of  $\text{ZrO}_2\text{-}2\text{Na}_2\text{ZrCl}_5\text{F}$  are plotted and compared with those of  $\text{Na}_2\text{ZrCl}_6$  and  $\text{Na}_2\text{ZrCl}_5\text{F}$  in Figures S6 and 2d, respectively; the results are summarized in Table S3. The positions of the absorption edges between  $\text{Na}_2\text{ZrCl}_6$  and  $\text{ZrO}_2$  in the Zr K-edge XANES spectra confirmed the tetravalent oxidation state of Zr in both  $\text{Na}_2\text{ZrCl}_5\text{F}$  and  $\text{ZrO}_2\text{-}2\text{Na}_2\text{ZrCl}_5\text{F}$ .<sup>24,29,31</sup> Notably, the absorption edges of  $\text{Na}_2\text{ZrCl}_5\text{F}$  and  $\text{ZrO}_2\text{-}2\text{Na}_2\text{ZrCl}_5\text{F}$  shifted toward higher energies compared to those of  $\text{Na}_2\text{ZrCl}_6$ , signifying the presence of Zr–F and Zr–O bonds. Furthermore, an increase in the absorption edge intensity was observed for  $\text{Na}_2\text{ZrCl}_5\text{F}$  and  $\text{ZrO}_2\text{-}2\text{Na}_2\text{ZrCl}_5\text{F}$  compared to  $\text{Na}_2\text{ZrCl}_6$ , which can be attributed to the presence of shorter Zr–O/F bonds and tetragonal- $\text{ZrO}_2$  (t- $\text{ZrO}_2$ ) with a higher coordination number. Typically, the pre-edge in XANES appears strong when the centrosymmetry collapses;<sup>56</sup> however, that of  $\text{ZrO}_2\text{-}2\text{Na}_2\text{ZrCl}_5\text{F}$  does not intensify despite the formation of a t- $\text{ZrO}_2$  structure with distorted polyhedra. This might be due to the minimal energy difference between the  $1s \rightarrow nd$  and  $1s \rightarrow np$  states in the Zr K-edge, in addition to a relatively small amount of the t- $\text{ZrO}_2$  phase compared to  $\text{Na}_2\text{ZrCl}_5\text{F}$ .<sup>57</sup> The appearance of the Zr–O peak at 1.5 Å in the EXAFS spectra (Figure 2d) verifies the formation of nanosized  $\text{ZrO}_2$  in the  $\text{ZrO}_2\text{-}2\text{Na}_2\text{ZrCl}_5\text{F}$  HNSE, corroborating the cryo-STEM results (Figures 2c and S5). The EXAFS fitting in the presence of t- $\text{ZrO}_2$  as a structural model resulted in a reasonable R value (1.3%), validating the presence of t- $\text{ZrO}_2$ . Moreover, the Debye–Waller factor for  $\text{ZrO}_2\text{-}2\text{Na}_2\text{ZrCl}_5\text{F}$  was higher than

those for both  $\text{Na}_2\text{ZrCl}_6$  and  $\text{Na}_2\text{ZrCl}_5\text{F}$ , suggesting that  $\text{ZrO}_2\text{-}2\text{Na}_2\text{ZrCl}_5\text{F}$  was either nanosized or amorphized (Table S3).

Figures 2e and S7 display the PDF results for  $\text{ZrO}_2\text{-}2\text{Na}_2\text{ZrCl}_5\text{F}$  compared with those for  $\text{Na}_2\text{ZrCl}_6$  and  $\text{Na}_2\text{ZrCl}_5\text{F}$  (Figures S1 and 2). Qualitative analysis up to 6 Å indicates that  $\text{ZrO}_2\text{-}2\text{Na}_2\text{ZrCl}_5\text{F}$  exhibits distinct characteristics of both  $\text{Na}_2\text{ZrCl}_5\text{F}$  and  $\text{t-ZrO}_2$ , in addition to minor NaCl impurities (Figure 2e). The complex oscillations between 3 and 5 Å lead to speculation that  $\text{ZrO}_2\text{-}2\text{Na}_2\text{ZrCl}_5\text{F}$  features a partially O-substituted interphase, consistent with the findings in our previous reported study.<sup>29</sup> Meanwhile, in cases where atomic arrangements lack consecutive sequences, PDF peaks tend to lose intensity across the entire  $r$ -range and eventually converge to 0.<sup>58,59</sup> Notably, for  $\text{ZrO}_2\text{-}2\text{Na}_2\text{ZrCl}_5\text{F}$  (Figure S7), the PDF peaks exhibited rapid attenuation from significantly lower  $r$ -ranges compared to those of  $\text{Na}_2\text{ZrCl}_6$  and  $\text{Na}_2\text{ZrCl}_5\text{F}$ . This suggests that the domains in  $\text{ZrO}_2\text{-}2\text{Na}_2\text{ZrCl}_5\text{F}$  are significantly nanosized and lack structural coherence over long  $r$ -ranges, coinciding with the XRD and XAS results. Unfortunately, attempts to conduct a PDF fitting analysis for  $\text{ZrO}_2\text{-}2\text{Na}_2\text{ZrCl}_5\text{F}$  to explore its long-range structural characteristics have been unsuccessful because of the lack of a model interphase structure.

The electrochemical stability of  $\text{ZrO}_2\text{-}2\text{Na}_2\text{ZrCl}_5\text{F}$  HNSE was evaluated using cyclic voltammetry (CV) on an SE-C mixture electrode in  $\text{Na}_3\text{Sn}|\text{Na}_3\text{PS}_4|(\text{SE-C})$  cells at 30 °C. Figures 3a and 3b show the first and second scan voltage

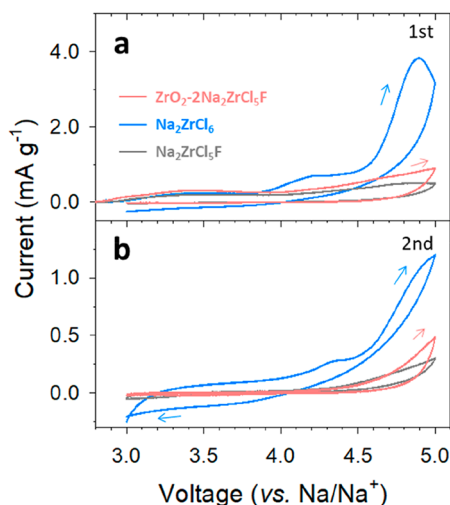


**Figure 3.** Cyclic voltammograms for  $\text{Na}_3\text{Sn}|\text{Na}_3\text{PS}_4|(\text{SE-C})$  cells at 30 °C for  $\text{ZrO}_2\text{-}2\text{Na}_2\text{ZrCl}_5\text{F}$  (red),  $\text{Na}_2\text{ZrCl}_5\text{F}$  (gray), and  $\text{Na}_2\text{ZrCl}_6$  (blue). (a) First and (b) second CV profiles at 0.1  $\text{mV s}^{-1}$ .

profiles of  $\text{Na}_2\text{ZrCl}_6$ ,  $\text{Na}_2\text{ZrCl}_5\text{F}$ , and  $\text{ZrO}_2\text{-}2\text{Na}_2\text{ZrCl}_5\text{F}$ , respectively.  $\text{Na}_2\text{ZrCl}_6$  exhibits a minor oxidative response up to 3.9 V (vs  $\text{Na}/\text{Na}^+$ ), with an intense oxidation reaction initiating at 4.6 V (vs  $\text{Na}/\text{Na}^+$ ). In contrast,  $\text{Na}_2\text{ZrCl}_5\text{F}$  and  $\text{ZrO}_2\text{-}2\text{Na}_2\text{ZrCl}_5\text{F}$  demonstrate minor oxidation currents up to 5.0 V (vs  $\text{Na}/\text{Na}^+$ ). In addition, the integrated oxidation currents up to 5.0 V (vs  $\text{Na}/\text{Na}^+$ ) for  $\text{Na}_2\text{ZrCl}_5\text{F}$  and  $\text{ZrO}_2\text{-}2\text{Na}_2\text{ZrCl}_5\text{F}$  are significantly lower ( $0.77 \text{ mA V g}^{-1}$  for  $\text{Na}_2\text{ZrCl}_5\text{F}$  and  $1.16 \text{ mA V g}^{-1}$  for  $\text{ZrO}_2\text{-}2\text{Na}_2\text{ZrCl}_5\text{F}$ ), compared to  $\text{Na}_2\text{ZrCl}_6$  ( $2.52 \text{ mA V g}^{-1}$ ). Furthermore,  $\text{Na}_2\text{ZrCl}_6$  exhibited cathodic signals that are particularly pronounced in the second negative scan, which is a

characteristic absent in  $\text{Na}_2\text{ZrCl}_5\text{F}$  and  $\text{ZrO}_2\text{-}2\text{Na}_2\text{ZrCl}_5\text{F}$ , thus confirming their superior electrochemical stability compared to  $\text{Na}_2\text{ZrCl}_6$  and highlighting the beneficial impact of fluorination.

To assess the effectiveness of  $\text{ZrO}_2\text{-}2\text{Na}_2\text{ZrCl}_5\text{F}$  in 5 V-class ASNBS, we prepared  $(\text{NaNCM-SE-C})|\text{Na}_3\text{PS}_4|\text{Na}_3\text{Sn}$  all-solid-state cells and compared their performance with cells utilizing  $\text{Na}_2\text{ZrCl}_6$  and  $\text{Na}_2\text{ZrCl}_5\text{F}$  at 30 °C. The cells were charged at 0.1 C ( $0.12 \text{ mA cm}^{-2}$ ) with a constant current–constant voltage mode (CCCV, a limiting current of  $0.012 \text{ mA cm}^{-2}$ ) and discharged at 0.1 C between 1.5 and 5.0 V (vs  $\text{Na}/\text{Na}^+$ ). The results are presented in Figure 4 and Table S4. The

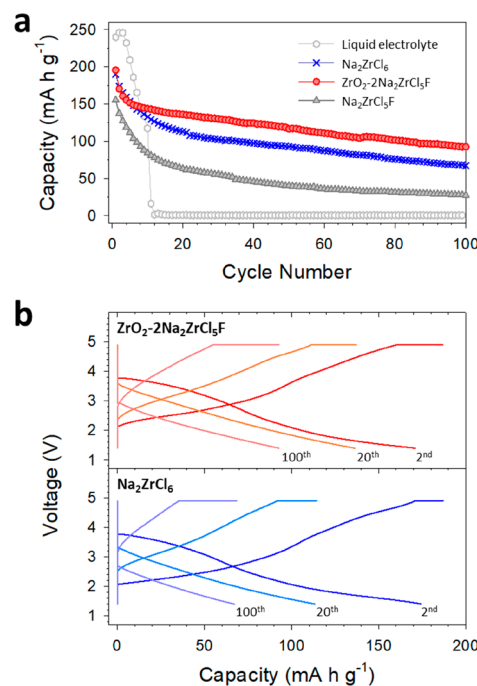


**Figure 4.** Electrochemical performance of  $\text{Na}_3\text{Sn}|\text{Na}_{0.66}\text{Ni}_{0.1}\text{Co}_{0.1}\text{Mn}_{0.8}\text{O}_2$  all-solid-state  $\text{Na}^+$  batteries (ASNBS) employing  $\text{ZrO}_2\text{-}2\text{Na}_2\text{ZrCl}_5\text{F}$ ,  $\text{Na}_2\text{ZrCl}_5\text{F}$ , and  $\text{Na}_2\text{ZrCl}_6$  at 0.1C and 30 °C. (a) Cycling performance and (b) corresponding charge–discharge voltage profiles. Voltage profiles and Coulombic efficiency of cells are displayed in Figures S8–S11.

cycling performance and corresponding charge–discharge voltage profiles at different cycles are presented in Figure 4a,b. Notably, the  $\text{NaNCM}|\text{Na}$  half-cell with a commercial liquid electrolyte (1 M  $\text{NaPF}_6$  in a 97:3 volume ratio mixture of propylene carbonate and fluoroethylene carbonate) exhibits poor reversibility (Figures 4a and S8). In contrast, ASNBS with halide SEs demonstrated relatively decent reversibility despite gradual capacity fading, which can be ascribed to (i) interfacial electrochemical and (electro)chemomechanical degradation and (ii) the degradation of bulk  $\text{NaNCM}$ . For  $\text{NaNCM}$ , a structural transition involving P'2 phase formation and vacancy ordering contributes to capacity fading when operated between 1.5 and 5.0 V (vs  $\text{Na}/\text{Na}^+$ ).<sup>60,61</sup> The ASNBS cells demonstrated high initial discharge capacities of 196 and 190  $\text{mA h g}^{-1}$  for  $\text{ZrO}_2\text{-}2\text{Na}_2\text{ZrCl}_5\text{F}$  and  $\text{Na}_2\text{ZrCl}_6$ , respectively. These comparable values correlate with their similar  $\text{Na}^+$  conductivities ( $2.1 \times 10^{-5}$  and  $1.1 \times 10^{-5} \text{ S cm}^{-1}$  for  $\text{ZrO}_2\text{-}2\text{Na}_2\text{ZrCl}_5\text{F}$  and  $\text{Na}_2\text{ZrCl}_6$ , respectively). However,  $\text{ZrO}_2\text{-}2\text{Na}_2\text{ZrCl}_5\text{F}$  demonstrated a higher capacity retention than  $\text{Na}_2\text{ZrCl}_6$ . Although

the initial discharge capacities and capacity fading (from the second to fifth cycles) were comparable for both, the capacity fading for  $\text{ZrO}_2\text{-}2\text{Na}_2\text{ZrCl}_5\text{F}$  was mitigated after the sixth cycle, in contrast to the continuous fading observed for  $\text{Na}_2\text{ZrCl}_6$ . Concurrently, the overpotential in the charge–discharge profile of  $\text{Na}_2\text{ZrCl}_6$  exceeded that of  $\text{ZrO}_2\text{-}2\text{Na}_2\text{ZrCl}_5\text{F}$  after the 20th cycle (Figure S9), indicating that the interfacial stability effect became more pronounced. The superior cycling stability of  $\text{ZrO}_2\text{-}2\text{Na}_2\text{ZrCl}_5\text{F}$  suggests a more stable nature and faster formation of passivating interfaces compared to  $\text{Na}_2\text{ZrCl}_6$ .<sup>29,50</sup> Consistently,  $\text{ZrO}_2\text{-}2\text{Na}_2\text{ZrCl}_5\text{F}$  demonstrated superior Coulombic efficiencies, averaging 97.93% from the second to the 20th cycles vs 97.36% for  $\text{Na}_2\text{ZrCl}_6$  (Figure S10).

However, despite the CV results confirming the superior oxidative stability of  $\text{Na}_2\text{ZrCl}_5\text{F}$  over  $\text{Na}_2\text{ZrCl}_6$  (Figure 3), the observed poorer cycle retention and Coulombic efficiency for  $\text{Na}_2\text{ZrCl}_5\text{F}$ , as compared to  $\text{Na}_2\text{ZrCl}_6$ , are noteworthy (Figures 4a and S10). This discrepancy can be attributed to the cycling test protocol, specifically the CCCV charging mode. The significantly lower ionic conductivity of  $\text{Na}_2\text{ZrCl}_5\text{F}$  ( $2.0 \times 10^{-7} \text{ S cm}^{-1}$ ) compared to  $\text{Na}_2\text{ZrCl}_6$  ( $1.1 \times 10^{-5} \text{ S cm}^{-1}$ ) or  $\text{ZrO}_2\text{-}2\text{Na}_2\text{ZrCl}_5\text{F}$  ( $2.1 \times 10^{-5} \text{ S cm}^{-1}$ ) led to the cells employing  $\text{Na}_2\text{ZrCl}_5\text{F}$  spending considerably more time at the constant voltage of 5.0 V (vs  $\text{Na}/\text{Na}^+$ ), as found in Figure S11. For example, during the first charging phase, the period spent at constant voltage was 420 min for  $\text{Na}_2\text{ZrCl}_5\text{F}$ , much longer than 215 min for  $\text{Na}_2\text{ZrCl}_6$  or 238 min for  $\text{ZrO}_2\text{-}2\text{Na}_2\text{ZrCl}_5\text{F}$ . This extended duration at high voltage exacerbated side reactions, thereby leading to capacity fading. These findings suggest the limitation of solely relying on fluorination to achieve the desired high-voltage stability of as high as 5 V (vs  $\text{Na}/\text{Na}^+$ ) and emphasize the necessity of addressing the compromised ionic conductivity caused by fluorination through the HNSE strategy.

To quantify the cathode–SE interfacial stability in  $\text{NaNCM}|\text{Na}_3\text{PS}_4|\text{Na}_3\text{Sn}$  cells, electrochemical impedance spectroscopy (EIS) analyses were conducted, and the results are summarized in Figure 5a,b. In the Nyquist plots (Figure 5a), an incomplete

high-frequency semicircle and a full midfrequency semicircle are observed, representing the resistances of the  $\text{Na}_3\text{PS}_4$  separating layer and the cathode–halide SE interfaces, respectively.<sup>16,24,31,62</sup> The results fitted with the equivalent circuit model (Figure S12) are displayed in Figure 5b and listed in Table S5. The comparable  $R_1 + R_2$  amplitudes for both cells (approximately 1200–1600  $\Omega$ ) are attributed to the use of identical  $\text{Na}_3\text{PS}_4$  SE layers. In the second cycle, the cell with  $\text{Na}_2\text{ZrCl}_6$  exhibited a lower  $R_3$  value (42.2  $\Omega$ ) compared to the  $\text{ZrO}_2\text{-}2\text{Na}_2\text{ZrCl}_5\text{F}$  cell (122.6  $\Omega$ ), despite the latter's slightly higher ionic conductivity ( $2.1 \times 10^{-5}$  vs  $1.1 \times 10^{-5} \text{ S cm}^{-1}$ ). This discrepancy is likely due to the contact hindrance with  $\text{NaNCM}$  particles caused by  $\text{ZrO}_2$  in the HNSE particles.<sup>26</sup> Notably, the  $R_3$  value of  $\text{Na}_2\text{ZrCl}_6$  exceeded that of  $\text{ZrO}_2\text{-}2\text{Na}_2\text{ZrCl}_5\text{F}$  after the 5th to 10th cycles, culminating in a substantially larger value at the 20th cycle: 947 vs 1461  $\Omega$ . This trend aligns well with the cycling performance behavior observed in Figures 4, S9, and S10.

In summary, the newly developed  $\text{Na}^+$ -conducting fluorinated HNSE  $\text{ZrO}_2\text{-}2\text{Na}_2\text{ZrCl}_5\text{F}$  was synthesized using a mechanochemical method and demonstrated an  $\text{Na}^+$  conductivity of  $2.1 \times 10^{-5} \text{ S cm}^{-1}$  at 30 °C. HNSEs comprising  $\text{ZrO}_2$  nanoparticles embedded in an amorphous  $\text{Na}_2\text{ZrCl}_5\text{F}$  matrix with the evolution of a potential O-substituted interphase were formed by reacting  $\text{Na}_2\text{O}$  with the metal halide precursors— $\text{ZrCl}_4$  and  $\text{ZrF}_4$ . The HNSE nanostructures were confirmed through synergistic structural analyses, which included synchrotron XAS, PDF, and cryo-STEM. Fluorination in  $\text{Na}_2\text{ZrCl}_6$  led to a significant decrease in ionic conductivity from  $1.1 \times 10^{-5}$  to  $2.0 \times 10^{-7} \text{ S cm}^{-1}$  in  $\text{Na}_2\text{ZrCl}_5\text{F}$ . Synchrotron PDF analysis revealed the underlying mechanism, which was characterized by the higher occupation of the Zr2-site over the Zr3-site in the  $P\bar{3}m1$  structure and the absence of a highly conductive  $P2_1/n$  phase. However, by implementing an interfacial conduction strategy in the HNSEs, the  $\text{Na}^+$  conductivity of  $\text{Na}_2\text{ZrCl}_5\text{F}$  increased by approximately 2 orders of magnitude. This improvement was attributed to enhanced interfacial  $\text{Na}^+$  transport in the  $\text{ZrO}_2\text{-}2\text{Na}_2\text{ZrCl}_5\text{F}$  nanostructures. The electrochemical oxidative stability of  $\text{ZrO}_2\text{-}2\text{Na}_2\text{ZrCl}_5\text{F}$  was significantly enhanced, exhibiting stability up to 5 V (vs  $\text{Na}/\text{Na}^+$ ), as evidenced by the CV results. The efficacy of  $\text{ZrO}_2\text{-}2\text{Na}_2\text{ZrCl}_5\text{F}$  in enabling 5 V-class cathode  $\text{NaNCM}$  in ASNBs was successfully demonstrated. Our results provide invaluable insights into the design of high-voltage superionic conductors and contribute to advancing the field of high-performance all-solid-state batteries.

## ASSOCIATED CONTENT

### Supporting Information

The Supporting Information is available free of charge at <https://pubs.acs.org/doi/10.1021/acsenergylett.4c00490>.

Experimental methods, PDF refinement profiles, crystal structures of  $\text{Na}_2\text{ZrCl}_6$  and  $\text{Na}_2\text{ZrCl}_5\text{F}$  with  $P\bar{3}m1$  and  $P2_1/n$  space groups, results of  $\text{ZrO}_2\text{-NaCl-Na}_2\text{ZrCl}_5\text{F}$  HNSEs with fixed volume fraction of  $\text{Na}_2\text{ZrCl}_5\text{F}$  (Nyquist Plots, Arrhenius plots,  $\text{Na}^+$  conductivity, activation energy, and XRD profiles), STEM EDXS images, XANES spectra, electrochemical performances of liquid electrolyte cells and ASNB cells using  $\text{NaNCM}$ , equivalent circuit, detailed characteristics of HNSEs, EXAFS fitting results, and fitted EIS results (PDF)

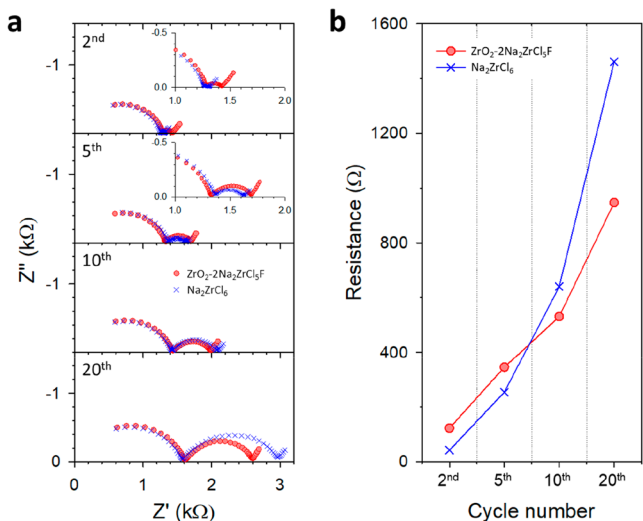


**Figure 5.** EIS results of  $\text{Na}_3\text{Sn}|\text{Na}_{0.66}\text{Ni}_{0.1}\text{Co}_{0.1}\text{Mn}_{0.8}\text{O}_2$  ASNB cells employing  $\text{Na}_2\text{ZrCl}_6$  or  $\text{ZrO}_2\text{-}2\text{Na}_2\text{ZrCl}_5\text{F}$  HNSE at 30 °C. (a) Nyquist plots at 2<sup>nd</sup>, 5<sup>th</sup>, 10<sup>th</sup>, and 20<sup>th</sup> cycles. (b) Fitted resistance as a function of cycle number.

## AUTHOR INFORMATION

## Corresponding Authors

Kyung-Wan Nam – Department of Energy and Materials Engineering, Dongguk University, Seoul 04620, South Korea; [orcid.org/0000-0001-6278-6369](https://orcid.org/0000-0001-6278-6369); Email: [knam@dongguk.edu](mailto:knam@dongguk.edu)

Yoon Seok Jung – Department of Chemical and Biomolecular Engineering, Yonsei University, Seoul 03722, South Korea; Email: [yoonsjung@yonsei.ac.kr](mailto:yoonsjung@yonsei.ac.kr)

## Authors

Juhyoun Park – Department of Chemical and Biomolecular Engineering, Yonsei University, Seoul 03722, South Korea

Daseul Han – Department of Energy and Materials Engineering, Dongguk University, Seoul 04620, South Korea

Jun Pyo Son – Department of Chemical and Biomolecular Engineering, Yonsei University, Seoul 03722, South Korea

Hiram Kwak – Department of Chemical and Biomolecular Engineering, Yonsei University, Seoul 03722, South Korea

Wonseok Ko – Department of Energy Science, Sungkyunkwan University (SKKU), Suwon 440-746, South Korea; SKKU Institute of Energy Science and Technology (SIEST), Sungkyunkwan University, Suwon 16419, South Korea

Changhyun Park – School of Energy and Chemical Engineering, Ulsan National Institute of Science and Technology (UNIST), Ulsan 44919, South Korea

Chanhee Lee – School of Energy and Chemical Engineering, Ulsan National Institute of Science and Technology (UNIST), Ulsan 44919, South Korea

Hyun-Wook Lee – School of Energy and Chemical Engineering, Ulsan National Institute of Science and Technology (UNIST), Ulsan 44919, South Korea; [orcid.org/0000-0001-9074-1619](https://orcid.org/0000-0001-9074-1619)

Jongsoo Kim – Department of Energy Science, Sungkyunkwan University (SKKU), Suwon 440-746, South Korea; SKKU Institute of Energy Science and Technology (SIEST), Sungkyunkwan University, Suwon 16419, South Korea

Complete contact information is available at:

<https://pubs.acs.org/10.1021/acseenergylett.4c00490>

## Author Contributions

<sup>†</sup>J.P. and D.H. contributed equally.

## Notes

The authors declare no competing financial interest.

## ACKNOWLEDGMENTS

This work was supported by the Samsung Science and Technology Foundation under project no. SRFC-MA2102-03 and by the National Research Foundation of Korea (NRF), funded by the Ministry of Science, ICT & Future Planning (2022M3J1A1085397). The PDF research used beamline 28-ID-1 (PDF) of the National Synchrotron Light Source II, a US Department of Energy (DOE) Office of Science User Facility operated for the DOE Office of Science by Brookhaven National Laboratory under contract no. DE-SC0012704. Y.S.J. is grateful to Prof. Dong-Hwa Seo and Jae-Seung Kim at KAIST for fruitful discussions.

## REFERENCES

- (1) Hannan, M.; Hoque, M. M.; Mohamed, A.; Ayob, A. Review of energy storage systems for electric vehicle applications: Issues and challenges. *Renew. & Sus. Energy Rev.* **2017**, *69*, 771–789.
- (2) Goodenough, J. B.; Kim, Y. Challenges for rechargeable Li batteries. *Chem. Mater.* **2010**, *22*, 587–603.
- (3) Dunn, B.; Kamath, H.; Tarascon, J.-M. Electrical energy storage for the grid: a battery of choices. *Science* **2011**, *334*, 928–935.
- (4) Hwang, J.-Y.; Myung, S.-T.; Sun, Y.-K. Sodium-ion batteries: present and future. *Chem. Soc. Rev.* **2017**, *46*, 3529–3614.
- (5) Abraham, K. M. How comparable are sodium-ion batteries to lithium-ion counterparts? *ACS Energy Lett.* **2020**, *5*, 3544–3547.
- (6) Fleischmann, J.; Hanike, M.; Horetsky, E.; Ibrahim, D.; Jautelat, S.; Linder, M.; Schaufuss, P.; Torscht, L.; van de Rijt, A. *Battery 2030: Resilient, sustainable, and circular*; McKinsey & Company, 2023; pp 218
- (7) Wang, J.; Yamada, Y.; Sodeyama, K.; Watanabe, E.; Takada, K.; Tateyama, Y.; Yamada, A. Fire-extinguishing organic electrolytes for safe batteries. *Nat. Energy* **2018**, *3*, 22–29.
- (8) Liu, K.; Liu, Y.; Lin, D.; Pei, A.; Cui, Y. Materials for lithium-ion battery safety. *Sci. Adv.* **2018**, *4*, No. eaas9820.
- (9) Liu, Y. K.; Zhao, C. Z.; Du, Z.; Zhang, X. Q.; Chen, A. B.; Zhang, Q. Research Progresses of Liquid Electrolytes in Lithium-Ion Batteries. *Small* **2023**, *19*, 2205315.
- (10) Stephenson, T.; Li, Z.; Olsen, B.; Mitlin, D. Lithium ion battery applications of molybdenum disulfide (MoS<sub>2</sub>) nanocomposites. *Energy Environ. Sci.* **2014**, *7*, 209–231.
- (11) Banerjee, A.; Park, K. H.; Heo, J. W.; Nam, Y. J.; Moon, C. K.; Oh, S. M.; Hong, S. T.; Jung, Y. S. Na<sub>3</sub>SbS<sub>4</sub>: a solution processable sodium superionic conductor for all-solid-state sodium-ion batteries. *Angew. Chem., Int. Ed.* **2016**, *128*, 9786–9790.
- (12) Duchêne, L.; Kühnel, R.-S.; Stilp, E.; Reyes, E. C.; Remhof, A.; Hagemann, H.; Battaglia, C. A stable 3 V all-solid-state sodium-ion battery based on a closo-borate electrolyte. *Energy Environ. Sci.* **2017**, *10*, 2609–2615.
- (13) Kim, J. J.; Yoon, K.; Park, I.; Kang, K. Progress in the development of sodium-ion solid electrolytes. *Small Methods* **2017**, *1*, 1700219.
- (14) Zhao, C.; Liu, L.; Qi, X.; Lu, Y.; Wu, F.; Zhao, J.; Yu, Y.; Hu, Y. S.; Chen, L. Solid-state sodium batteries. *Adv. Energy Mater.* **2018**, *8*, 1703012.
- (15) Lu, Y.; Li, L.; Zhang, Q.; Niu, Z.; Chen, J. Electrolyte and interface engineering for solid-state sodium batteries. *Joule* **2018**, *2*, 1747–1770.
- (16) Park, J.; Son, J. P.; Ko, W.; Kim, J.-S.; Choi, Y.; Kim, H.; Kwak, H.; Seo, D.-H.; Kim, J.; Jung, Y. S. NaAlCl<sub>4</sub>: New Halide Solid Electrolyte for 3 V Stable Cost-Effective All-Solid-State Na-Ion Batteries. *ACS Energy Lett.* **2022**, *7*, 3293–3301.
- (17) Chen, S.; Wu, C.; Shen, L.; Zhu, C.; Huang, Y.; Xi, K.; Maier, J.; Yu, Y. Challenges and perspectives for NASICON-type electrode materials for advanced sodium-ion batteries. *Adv. Mater.* **2017**, *29*, 1700431.
- (18) Hayashi, A.; Noi, K.; Sakuda, A.; Tatsumisago, M. Superionic glass-ceramic electrolytes for room-temperature rechargeable sodium batteries. *Nat. Commun.* **2012**, *3*, 856.
- (19) Chen, S.; Xie, D.; Liu, G.; Mwizerwa, J. P.; Zhang, Q.; Zhao, Y.; Xu, X.; Yao, X. Sulfide solid electrolytes for all-solid-state lithium batteries: Structure, conductivity, stability and application. *Energy Storage Mater.* **2018**, *14*, 58–74.
- (20) Fuchs, T.; Culver, S. P.; Till, P.; Zeier, W. G. Defect-mediated conductivity enhancements in Na<sub>3-x</sub>Pn<sub>1-x</sub>W<sub>x</sub>S<sub>4</sub> (Pn = P, Sb) using aliovalent substitutions. *ACS Energy Lett.* **2020**, *5*, 146–151.
- (21) Wu, J.; Liu, S.; Han, F.; Yao, X.; Wang, C. Lithium/sulfide all-solid-state batteries using sulfide electrolytes. *Adv. Mater.* **2021**, *33*, 2000751.
- (22) Zhang, Q.; Cao, D.; Ma, Y.; Natan, A.; Aurora, P.; Zhu, H. Sulfide-based solid-state electrolytes: synthesis, stability, and potential for all-solid-state batteries. *Adv. Mater.* **2019**, *31*, 1901131.

- (23) Zhang, Q.; Zhang, C.; Hood, Z. D.; Chi, M.; Liang, C.; Jalarvo, N. H.; Yu, M.; Wang, H. Abnormally low activation energy in cubic  $\text{Na}_3\text{SbS}_4$  superionic conductors. *Chem. Mater.* **2020**, *32*, 2264–2271.
- (24) Kwak, H.; Lyoo, J.; Park, J.; Han, Y.; Asakura, R.; Remhof, A.; Battaglia, C.; Kim, H.; Hong, S.-T.; Jung, Y. S.  $\text{Na}_2\text{ZrCl}_6$  enabling highly stable 3 V all-solid-state Na-ion batteries. *Energy Storage Mater.* **2021**, *37*, 47–54.
- (25) Kwak, H.; Wang, S.; Park, J.; Liu, Y.; Kim, K. T.; Choi, Y.; Mo, Y.; Jung, Y. S. Emerging Halide Superionic Conductors for All-Solid-State Batteries: Design, Synthesis, and Practical Applications. *ACS Energy Lett.* **2022**, *7*, 1776–1805.
- (26) Duchêne, L.; Remhof, A.; Hagemann, H.; Battaglia, C. Status and prospects of hydroborate electrolytes for all-solid-state batteries. *Energy Storage Mater.* **2020**, *25*, 782–794.
- (27) Asano, T.; Sakai, A.; Ouchi, S.; Sakaida, M.; Miyazaki, A.; Hasegawa, S. Solid halide electrolytes with high lithium-ion conductivity for application in 4 V class bulk-type all-solid-state batteries. *Adv. Mater.* **2018**, *30*, 1803075.
- (28) Wang, S.; Bai, Q.; Nolan, A. M.; Liu, Y.; Gong, S.; Sun, Q.; Mo, Y. Lithium chlorides and bromides as promising solid-state chemistries for fast ion conductors with good electrochemical stability. *Angew. Chem., Int. Ed.* **2019**, *58*, 8039–8043.
- (29) Kwak, H.; Kim, J.-S.; Han, D.; Kim, J. S.; Park, J.; Kwon, G.; Bak, S.-M.; Heo, U.; Park, C.; Lee, H.-W.; Nam, K. W.; Seo, D. H.; Jung, Y. S. Boosting the interfacial superionic conduction of halide solid electrolytes for all-solid-state batteries. *Nat. Commun.* **2023**, *14*, 2459.
- (30) Liu, Z.; Ma, S.; Liu, J.; Xiong, S.; Ma, Y.; Chen, H. High ionic conductivity achieved in  $\text{Li}_3\text{Y}(\text{Br}_x\text{Cl}_3)$  mixed halide solid electrolyte via promoted diffusion pathways and enhanced grain boundary. *ACS Energy Lett.* **2021**, *6*, 298–304.
- (31) Kwak, H.; Han, D.; Lyoo, J.; Park, J.; Jung, S. H.; Han, Y.; Kwon, G.; Kim, H.; Hong, S. T.; Nam, K. W.; Jung, Y. S. New Cost-Effective Halide Solid Electrolytes for All-Solid-State Batteries: Mechanochemically Prepared  $\text{Fe}^{3+}$ -Substituted  $\text{Li}_2\text{ZrCl}_6$ . *Adv. Energy Mater.* **2021**, *11*, 2003190.
- (32) Park, J.; Han, D.; Kwak, H.; Han, Y.; Choi, Y. J.; Nam, K.-W.; Jung, Y. S. Heat treatment protocol for modulating ionic conductivity via structural evolution of  $\text{Li}_{3-x}\text{Yb}_{1-x}\text{M}_x\text{Cl}_6$  ( $\text{M} = \text{Hf}^{4+}, \text{Zr}^{4+}$ ) new halide superionic conductors for all-solid-state batteries. *Chem. Eng. J.* **2021**, *425*, 130630.
- (33) Kim, K.; Park, D.; Jung, H.-G.; Chung, K. Y.; Shim, J. H.; Wood, B. C.; Yu, S. Material design strategy for halide solid electrolytes  $\text{Li}_3\text{MX}_6$  ( $\text{X} = \text{Cl}, \text{Br}, \text{I}$ ) for all-solid-state high-voltage Li-ion batteries. *Chem. Mater.* **2021**, *33*, 3669–3677.
- (34) Kwak, H.; Han, D.; Son, J. P.; Kim, J. S.; Park, J.; Nam, K.-W.; Kim, H.; Jung, Y. S.  $\text{Li}^+$  conduction in aliovalent-substituted monoclinic  $\text{Li}_2\text{ZrCl}_6$  for all-solid-state batteries:  $\text{Li}_{2+x}\text{Zr}_{1-x}\text{M}_x\text{Cl}_6$  ( $\text{M} = \text{In}, \text{Sc}$ ). *Chem. Eng. J.* **2022**, *437*, 135413.
- (35) Kim, J. S.; Jung, S.; Kwak, H.; Han, Y.; Kim, S.; Lim, J.; Lee, Y. M.; Jung, Y. S. Synergistic halide-sulfide hybrid solid electrolytes for Ni-rich cathodes design guided by digital twin for all-solid-state Li batteries. *Energy Storage Mater.* **2023**, *55*, 193–204.
- (36) Li, X.; Liang, J.; Yang, X.; Adair, K. R.; Wang, C.; Zhao, F.; Sun, X. Progress and perspectives on halide lithium conductors for all-solid-state lithium batteries. *Energy Environ. Sci.* **2020**, *13*, 1429–1461.
- (37) Liang, J.; Li, X.; Wang, S.; Adair, K. R.; Li, W.; Zhao, Y.; Wang, C.; Hu, Y.; Zhang, L.; Zhao, S.; Lu, S.; Huang, H.; Li, R.; Mo, Y.; Sun, X. Site-Occupation-Tuned Superionic  $\text{Li}_x\text{ScCl}_{3+x}$  Halide Solid Electrolytes for All-Solid-State Batteries. *J. Am. Chem. Soc.* **2020**, *142*, 7012–7022.
- (38) Li, X.; Liang, J.; Luo, J.; Norouzi Banis, M.; Wang, C.; Li, W.; Deng, S.; Yu, C.; Zhao, F.; Hu, Y.; Sham, T.-K.; Zhang, L.; Zhao, S.; Lu, S.; Huang, H.; Li, R.; Adair, K. R.; Sun, X. Air-stable  $\text{Li}_3\text{InCl}_6$  electrolyte with high voltage compatibility for all-solid-state batteries. *Energy Environ. Sci.* **2019**, *12*, 2665–2671.
- (39) Park, K.-H.; Kaup, K.; Assoud, A.; Zhang, Q.; Wu, X.; Nazar, L. F. High-voltage superionic halide solid electrolytes for all-solid-state Li-ion batteries. *ACS Energy Lett.* **2020**, *5*, 533–539.
- (40) Schlem, R.; Muiy, S.; Prinz, N.; Banik, A.; Shao-Horn, Y.; Zobel, M.; Zeier, W. G. Mechanochemical synthesis: a tool to tune cation site disorder and ionic transport properties of  $\text{Li}_3\text{MCl}_6$  ( $\text{M} = \text{Y}, \text{Er}$ ) superionic conductors. *Adv. Energy Mater.* **2020**, *10*, 1903719.
- (41) Sebti, E.; Evans, H. A.; Chen, H.; Richardson, P. M.; White, K. M.; Giovine, R.; Koirala, K. P.; Xu, Y.; Gonzalez-Correa, E.; Wang, C.; Brown, C. M.; Cheetham, A. K.; Canepa, P.; Clément, R. J. Stacking faults assist lithium-ion conduction in a halide-based superionic conductor. *J. Am. Chem. Soc.* **2022**, *144*, 5795–5811.
- (42) Schlem, R.; Banik, A.; Eckardt, M.; Zobel, M.; Zeier, W. G.  $\text{Na}_{3-x}\text{Er}_{1-x}\text{Zr}_x\text{Cl}_6$ —A Halide-Based Fast Sodium-Ion Conductor with Vacancy-Driven Ionic Transport. *ACS Appl. Energy Mater.* **2020**, *3*, 10164–10173.
- (43) Wu, E. A.; Banerjee, S.; Tang, H.; Richardson, P. M.; Doux, J.-M.; Qi, J.; Zhu, Z.; Grenier, A.; Li, Y.; Zhao, E.; Deysher, G.; Sebti, E.; Nguyen, H.; Stephens, R.; Verbist, G.; Chapman, K. W.; Clément, R. J.; Banerjee, A.; Meng, Y. S.; Ong, S. P. A stable cathode-solid electrolyte composite for high-voltage, long-cycle-life solid-state sodium-ion batteries. *Nat. Commun.* **2021**, *12*, 1256.
- (44) Li, L.; Yao, J.; Xu, R.; Lin, Q.; Yan, X.; Yu, C.; Zhang, L. Highly stable and encapsulation-microstructural cathode derived by self-pressurization behavior in Na-halides-based all-solid-state batteries. *Energy Storage Mater.* **2023**, *63*, 103016.
- (45) Wang, L.; Song, Z.; Lou, X.; Chen, Y.; Wang, T.; Wang, Z.; Chen, H.; Yin, W.; Avdeev, M.; Kan, W. H.; Hu, B.; Luo, W.  $\text{Na}_{2.5}\text{Cr}_{0.5}\text{Zr}_{0.5}\text{Cl}_6$ : A New Halide-Based Fast Sodium-Ion Conductor. *Small* **2024**, *2400195*.
- (46) Okada, Y.; Kimura, T.; Motohashi, K.; Sakuda, A.; Hayashi, A. Mechanochemical Synthesis and Characterization of  $\text{Na}_{3-x}\text{In}_{1-x}\text{Zr}_x\text{Cl}_6$  Solid Electrolyte. *Electrochemistry* **2023**, *91*, 077009–077009.
- (47) Sebti, E.; Qi, J.; Richardson, P. M.; Ridley, P.; Wu, E. A.; Banerjee, S.; Giovine, R.; Cronk, A.; Ham, S.-Y.; Meng, Y. S.; Clément, R. J. Synthetic control of structure and conduction properties in Na-Y-Zr-Cl solid electrolytes. *J. Mater. Chem. A* **2022**, *10*, 21565–21578.
- (48) Meyer, G.; Peter Ax, S.; Schleid, T.; Irmmler, M. The chlorides  $\text{Na}_3\text{MCl}_6$  ( $\text{M} = \text{Eu-Lu}, \text{Y}, \text{Sc}$ ): Synthesis, crystal structures, and thermal behaviour. *Z. Anorg. Allg. Chem.* **1987**, *554*, 25–33.
- (49) Dai, T.; Wu, S.; Lu, Y.; Yang, Y.; Liu, Y.; Chang, C.; Rong, X.; Xiao, R.; Zhao, J.; Liu, Y.; Wang, W.; Chen, L.; Hu, Y. S. Inorganic glass electrolytes with polymer-like viscoelasticity. *Nat. Energy* **2023**, *8*, 1221–1228.
- (50) Fu, J.; Wang, S.; Wu, D.; Luo, J.; Wang, C.; Liang, J.; Lin, X.; Hu, Y.; Zhang, S.; Zhao, F.; Li, W.; Li, M.; Duan, H.; Zhao, Y.; Gu, M.; Sham, T.-K.; Mo, Y.; Sun, X. Halide Heterogeneous Structure Boosting Ionic Diffusion and High-Voltage Stability of Sodium Superionic Conductors. *Adv. Mater.* **2024**, *36*, 2308012.
- (51) Lin, X.; Zhao, Y.; Wang, C.; Luo, J.; Fu, J.; Xiao, B.; Gao, Y.; Li, W.; Zhang, S.; Xu, J.; Yang, F.; Hao, X.; Duan, H.; Sun, Y.; Guo, J.; Huang, Y.; Sun, X. A Dual Anion Chemistry-Based Superionic Glass Enabling Long-Cycling All-Solid-State Sodium-Ion Batteries. *Angew. Chem., Int. Ed.* **2024**, *63*, e202314181.
- (52) Zhang, S.; Zhao, F.; Wang, S.; Liang, J.; Wang, J.; Wang, C.; Zhang, H.; Adair, K.; Li, W.; Li, M.; Duan, H.; Zhao, Y.; Yu, R.; Li, R.; Huang, H.; Zhang, L.; Zhao, S.; Lu, S.; Sham, T.-K.; Mo, Y.; Sun, X. Advanced High-Voltage All-Solid-State Li-Ion Batteries Enabled by a Dual-Halogen Solid Electrolyte. *Adv. Energy Mater.* **2021**, *11*, 2100836.
- (53) Zhang, L.; Yuan, T.; Soule, L.; Sun, H.; Pang, Y.; Yang, J.; Zheng, S. Enhanced Ionic Transport and Structural Stability of Nb-Doped  $\text{O}_3\text{-NaFe}_{0.55}\text{Mn}_{0.45-x}\text{Nb}_x\text{O}_2$  Cathode Material for Long-Lasting Sodium-Ion Batteries. *ACS Appl. Energy Mater.* **2020**, *3*, 3770–3778.
- (54) Lee, S.; Ko, W.; Park, H.; Lee, Y.; Kang, J.; Ahn, J.; Lee, S.; Sim, E.; Ihm, K.; Park, K.-Y.; Kim, J. Gradational anionic redox enabling high-energy P2-type Na-layered oxide cathode. *Chem. Eng. J.* **2023**, *451*, 138883.
- (55) Shannon, R. D. Revised effective ionic radii and systematic studies of interatomic distances in halides and chalcogenides. *Acta*

*Crystallogr. A: Cryst. Phys. Diffraction Theor. Gen. Crystallogr.* **1976**, *32*, 751–767.

(56) Li, P.; Chen, I.-W.; Penner-Hahn, J. E. X-ray-absorption studies of zirconia polymorphs. I. Characteristic local structures. *Phys. Rev. B* **1993**, *48*, 10063.

(57) Gaultois, M. W.; Greedan, J. E.; Grosvenor, A. P. Investigation of coordination changes in substituted transition-metal oxides by K-edge XANES: Beyond the pre-edge. *J. Electron Spectrosc. Relat. Phenom.* **2011**, *184*, 192–195.

(58) Petkov, V. Pair distribution functions analysis. *Charact. Mater.* **2012**, 1361–1372.

(59) Masadeh, A. S. Total scattering atomic pair distribution function: new methodology for nanostructure determination. *J. Exp. Nanosci.* **2016**, *11*, 951–974.

(60) You, Y.; Manthiram, A. Progress in high-voltage cathode materials for rechargeable sodium-ion batteries. *Adv. Energy Mater.* **2018**, *8*, 1701785.

(61) Hwang, J. Y.; Kim, J.; Yu, T. Y.; Sun, Y. K. A new P2-type layered oxide cathode with extremely high energy density for sodium-ion batteries. *Adv. Energy Mater.* **2019**, *9*, 1803346.

(62) Han, Y.; Jung, S. H.; Kwak, H.; Jun, S.; Kwak, H. H.; Lee, J. H.; Hong, S. T.; Jung, Y. S. Single- or poly-crystalline Ni-rich layered cathode, sulfide or halide solid electrolyte: which will be the winners for all-solid-state batteries? *Adv. Energy Mater.* **2021**, *11*, 2100126.